Physiological Measurement

PAPER

Robust QRS detection for HRV estimation from compressively sensed ECG measurements for remote health-monitoring systems

To cite this article: Jeevan K Pant and Sridhar Krishnan 2018 *Physiol. Meas.* **39** 035002

IOP Publishing Physiol. Meas. 39 (2018) 035002 (19pp) https://doi.org/10.1088/1361-6579/aaa3c9

Physiological Measurement

Institute of Physics and Engineering in Medicine

CrossMark

RECEIVED
22 August 2017

REVISED
18 December 2017

ACCEPTED FOR PUBLICATION
22 December 2017

PUBLISHED
15 March 2018

PAPER

Robust QRS detection for HRV estimation from compressively sensed ECG measurements for remote health-monitoring systems

Jeevan K Pant and Sridhar Krishnan

Department of Electrical and Computer Engineering, Ryerson University, Toronto, ON M5B 2K3, Canada

E-mail: jeevan1.pant@ryerson.ca **and** krishnan@ryerson.ca

Keywords: low power sensing, bio sensors, electrocardiogram signals, block-sparse structure, compressive sensing, heart rate variability, remote telemonitoring

Abstract

Objective: To present a new compressive sensing (CS)-based method for the acquisition of ECG signals and for robust estimation of heart-rate variability (HRV) parameters from compressively sensed measurements with high compression ratio. *Approach*: CS is used in the biosensor to compress the ECG signal. Estimation of the locations of QRS segments is carried out by applying two algorithms on the compressed measurements. The first algorithm reconstructs the ECG signal by enforcing a block-sparse structure on the first-order difference of the signal, so the transient QRS segments are significantly emphasized on the first-order difference of the signal. Multiple block-divisions of the signals are carried out with various block lengths, and multiple reconstructed signals are combined to enhance the robustness of the localization of the QRS segments. The second algorithm removes errors in the locations of QRS segments by applying low-pass filtering and morphological operations. *Main results*: The proposed CS-based method is found to be effective for the reconstruction of ECG signals by enforcing transient QRS structures on the first-order difference of the signal. It is demonstrated to be robust not only to high compression ratio but also to various artefacts present in ECG signals acquired by using on-body wireless sensors. HRV parameters computed by using the QRS locations estimated from the signals reconstructed with a compression ratio as high as 90% are comparable with that computed by using QRS locations estimated by using the Pan–Tompkins algorithm. *Significance*: The proposed method is useful for the realization of long-term HRV monitoring systems by using CS-based low-power wireless on-body biosensors.

1. Introduction

Healthcare expenditure is increasing worldwide, and it is expected to continue increasing in the future (National Health Expenditure Trends 2014, Purdy 2015). Remote wireless telemonitoring is emerging as a promising method for reducing healthcare expenses and for making healthcare services available to a large number of people (Jovanov *et al* 2005, Lin *et al* 2010, Gangopadhyay *et al* 2014). Biosensors used in such healthcare systems are desired to consume small amounts of on-chip resources and power (Goudar and Potkonjak 2013, Noshadi *et al* 2013). The compressive sensing (CS) technique (Donoho 2006, Candes and Tao 2006, Candes *et al* 2006) has been found to be effective for carrying out efficient signal compression for wireless telemonitoring of physiological signals for cardiovascular health monitoring (Mamaghanian *et al* 2011, Zhang *et al* 2013, Liu *et al* 2014).

Detection of QRS segments from electrocardiogram (ECG) signals has remained an active research area for over 30 years (Pan and Tompkins 1985, Köhler *et al* 2002, Arzeno *et al* 2008, Dipu and Lian 2015). The most well-known algorithm for QRS detection is the one proposed by Pan and Tompkins (Pan and Tompkins 1985). A modified version of the Pan–Tompkins algorithm was presented by Hamilton and Tompkins in Hamilton and Tompkins (1986). In the results presented in Pan and Tompkins (1985) and Hamilton and Tompkins (1986), the QRS detection performance for the Pan–Tompkins and Hamilton–Tompkins algorithms are comparable. Various other QRS detection algorithms have appeared in the literature (Xue *et al* 1992, Suppappola and Sun 1994, Arzeno *et al* 2008), however, the Pan–Tompkins and Hamilton–Tompkins algorithms have been well favoured for their simplicity and low computational cost.

Recently, CS-based low-power sensing for the acquisition of physiological signals has drawn the attention of the bio-sensing research community (Mamaghanian *et al* 2011, Dixon *et al* 2012, Liu *et al* 2014). The results presented in these papers apprise the readers of the effectiveness of CS for reducing power consumption in biosensors. However, the methods presented in Mamaghanian *et al* (2011), Liu *et al* (2014) and Dixon *et al* (2012) are based on applying the state-of-the-art signal reconstruction algorithms that are not tailored to the physiological signals. Hence, the maximum compression ratio (CR) with which the CS-based biosensor can be realized is limited to 50%–60%. In Pant and Krishnan (2013, 2014b), Pant and Krishnan (2016), signal reconstruction algorithms tailored and adapted to physiological signals are proposed and CS-based bio-sensing by using such algorithms is studied. In particular, the $\ell_{2/p}^{d}$-regularized least-squares ($\ell_{2/p}^{d}$-RLS) algorithm is proposed in Pant and Krishnan (2016), and it is shown to offer improved performance for the reconstruction of signals admitting a block-sparse structure in the first-order difference, such as foot-gait signals.

We propose a new CS-based method for the acquisition of ECG signals, which can be used for long-term telemonitoring of the sequence of RR-intervals, and thereby of the heart-rate variability (HRV), by using low-power biosensors. A CS-based HRV telemonitoring system can be implemented as shown in figure 1. The biosensor unit consists of (a) a transducer, which is marked as circle filled with black color, (b) a signal acquisition and preprocessing unit, (c) a signal compression based on CS, and (d) a wireless transmitter.

Conventional monitoring systems implement the signal compression unit based on the conventional signal compression techniques, whereas the CS-based systems implement the compression unit based on random projection. CS-based signal compression is computationally more efficient than the conventional signal compression methods. The measurements obtained by using CS are transmitted using a wireless channel to a receiver placed nearby the sensor unit. The measurements can be sent to the doctor's office through the internet. In the doctor's office, the measurements are received, and signal reconstruction and HRV parameter estimation carried out.

We focus our investigation on increasing the CR for the signal compression unit up to and more than 90%, and thereby reducing the amount of data transmitted through the wireless channel. In the proposed method, the CS procedure used in the biosensor is based on using a sparse measurement matrix, and associated signal reconstruction is carried out by using a variant of the $\ell_{2/p}^{d}$-regularized least-squares ($\ell_{2/p}^{d}$-RLS) algorithm proposed in Pant and Krishnan (2016), called the robust $\ell_{2/p}^{d}$-RLS algorithm. The $\ell_{2/p}^{d}$-RLS algorithm is based on modelling the signal as a sequence of signal blocks and promoting a block-sparse structure on the first-order difference of the signal (Pant and Krishnan 2016). In the robust $\ell_{2/p}^{d}$-RLS algorithm, the $\ell_{2/p}^{d}$-RLS algorithm is improved (a) for enhancing the transient structure of the QRS segments, and (b) for enhancing its robustness to the mismatch between the natural-block structure of the ECG signal and the block-structure modelled by the $\ell_{2/p}^{d}$-RLS algorithm. The robust $\ell_{2/p}^{d}$-RLS algorithm offers improved detection of the QRS segments from compressed measurements obtained with CR as high as 90% and more. Clinically relevant statistical and fractal parameters of the RR-interval time series of ECG signals, estimated by using the proposed CS-based method with CR $= 90\%$ and more, are comparable with, or better than, that estimated based on applying the Pan–Tompkins algorithm (Pan and Tompkins 1985).

The rest of the paper is organized as follows. In section 2, the state-of-the-art on the reconstruction of block-sparse signals and $\ell_{2/p}^{d}$-RLS algorithms is reviewed. In section 3, block-sparse modelling of ECG signals is discussed, and the proposed robust $\ell_{2/p}^{d}$-RLS algorithm is presented. Another algorithm for removing errors on the locations of QRS segments is also presented. Section 4 presents and discusses simulation results. Section 5 draws the conclusion.

2. Background and previous work

2.1. CS and recovery of block-sparse signals

Suppose a signal vector $\mathbf{x}$ of length N is divided into signal blocks $\mathbf{x}_1, \mathbf{x}_2, \ldots, \mathbf{x}_s$, each of length b, as

$$\mathbf{x} = \left[\mathbf{x}_1^T \; \mathbf{x}_2^T \; \cdots \; \mathbf{x}_s^T\right]^T, \tag{1}$$

where $Sb = N$. The vector $\mathbf{x}$ is said to be K-block sparse if K block vectors have non-zero energy and rest of the blocks have zero energy.

In CS, signal $\mathbf{x}$ and its measurement vector $\mathbf{y}$ of length M with $M \ll N$ are interrelated as

$$\mathbf{y} = \Phi\mathbf{x}, \tag{2}$$

where Φ is a measurement matrix of size $M \times N$.

Reconstruction of $\mathbf{x}$ from $\mathbf{y}$ can be carried out by solving the ℓ_1/ℓ_2-minimization problem

$$\begin{aligned} \underset{\mathbf{x}}{\text{minimize}} \quad & \|\mathbf{x}\|_{2/1} = \sum_{i=1}^{S} ||\mathbf{x}_i||_2 \\ \text{subject to:} \quad & \mathbf{y} = \Phi\mathbf{x} \end{aligned} \tag{3}$$

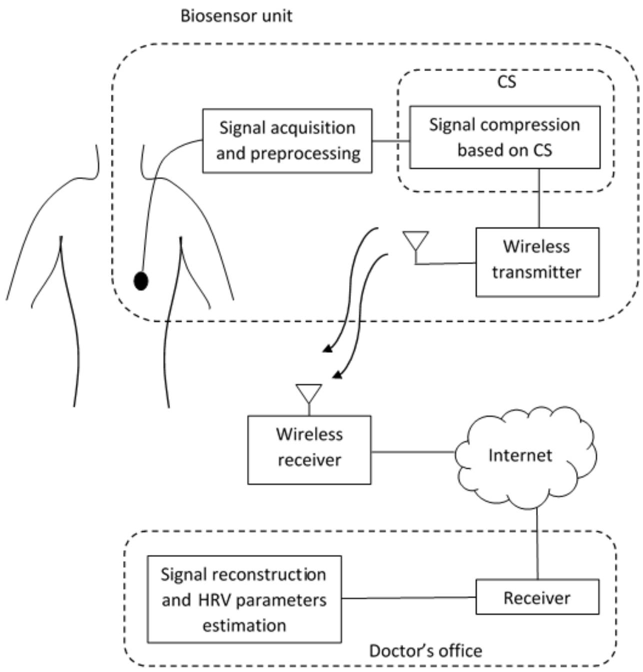

Figure 1. CS-based healthcare monitoring methodology.

where $||\mathbf{x}||_{2/1}$ is the ℓ_1/ℓ_2 norm of $\mathbf{x}$ (Stojnic *et al* 2009, Eldar and Mishali 2009, Eldar *et al* 2010).

2.2. $\ell^d_{2/p}$-RLS algorithm

A first-order difference $\mathbf{x}^d$ of a vector $\mathbf{x}$ of length $N+1$ can be obtained as

$$\mathbf{x}^d = \left[x^d_1 \; x^d_2 \; \cdots \; x^d_N\right]^T, \tag{4}$$

where $x^d_n = x_n - x_{n+1}$ for $n = 1, 2, \ldots, N$ and x_n is the nth component of $\mathbf{x}$. Suppose b is a positive integer and $S = N/b$ is also a positive integer. Vector $\mathbf{x}^d$ can be divided into blocks $\mathbf{x}^d_1, \mathbf{x}^d_2, \ldots, \mathbf{x}^d_s$ each of length b as

$$\mathbf{x}^d = \left[\left(\mathbf{x}^d_1\right)^T \; \left(\mathbf{x}^d_2\right)^T \; \cdots \; \left(\mathbf{x}^d_s\right)^T\right]^T. \tag{5}$$

The block-sparsity of $\mathbf{x}^d$ can be evaluated by using the $\ell^d_{2/p}$ function $f_r(\mathbf{x})$ given by

$$f_r(\mathbf{x}) = \left[\sum_{n=1}^{S}\left(\left|\left|\mathbf{x}^d_n\right|\right|_2\right)^p\right]^{1/p} \tag{6}$$

with $0 < p \leqslant 1$ (Pant and Krishnan 2016). Consequently, signal $\mathbf{x}$ can be reconstructed from its measurements $\mathbf{y}$ by solving the $\ell^d_{2/p}$-regularized least-squares ($\ell^d_{2/p}$-RLS) problem

$$\underset{\mathbf{x}}{\text{minimize}} \quad \tfrac{1}{2}\,||\Phi\mathbf{x} - \mathbf{y}||_2^2 + \lambda f_{r,\epsilon}(\mathbf{x}), \tag{7}$$

where the regularization function $f_{r,\epsilon}(\mathbf{x})$ is given by

$$f_{r,\epsilon}(\mathbf{x}) = \sum_{n=1}^{S}\left(\left|\left|\mathbf{x}^d_i\right|\right|_2^2 + \epsilon^2\right)^{p/2},$$

with $0 < p \leqslant 1$ (Pant and Krishnan 2016). The regularization parameter λ can be used to balance the trade-off between the block-sparse structure and the signal fidelity, and the parameter ϵ holds a small positive value, which can be used to facilitate the optimization; see Pant and Krishnan (2013, 2014b), Pant and Krishnan (2016) and Pant *et al* (2014).

The $\ell^d_{2/p}$-RLS algorithm presented in Pant and Krishnan (2016) is more generalized than the ℓ_1/ℓ_2 algorithm, in that it can be applied with a value of p suitable for the level of block sparsity. In the application studied in this paper, the $\ell^d_{2/p}$-RLS algorithm would be more effective because it can be applied with $p \approx 0$ in order to enhance the block-sparse structure.

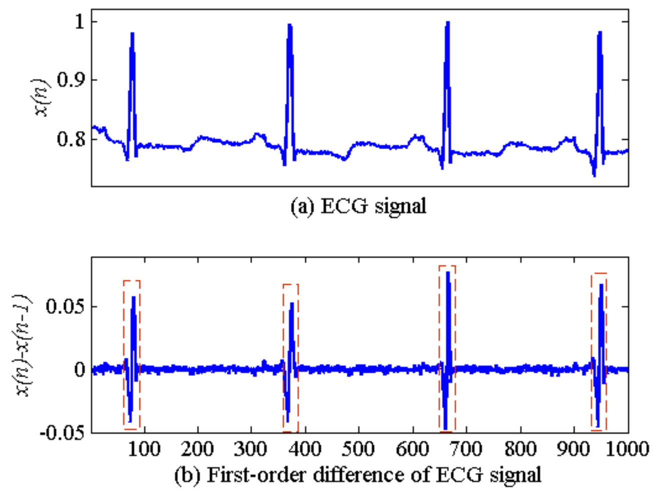

Figure 2. ECG signal with transient QRS structures.

3. Robust detection of QRS segments from CS measurements with high CR

3.1. ECG signal and its block representation

Consider the segment of an ECG signal shown in figure 2(a), which contains QRS spike structures. The variability of values of the components of the ECG signal in between any two succeeding QRS spikes is very low. Consequently, the first-order difference of such signals would admit a near-block-sparse structure, as shown in figure 2(b).

In the block-sparse representation of the first-order difference $\mathbf{x}^d$ carried out as in (5), the segment of $\mathbf{x}^d$ consisting of consecutive significant valued components can be called as the *significant-natural* blocks, and that consisting of consecutive insignificant components can be called as the *insignificant-natural* blocks. The block vectors from among $\tilde{\mathbf{x}}_1, \tilde{\mathbf{x}}_2, \ldots, \tilde{\mathbf{x}}_s$ that constitute a significant-natural block, will be called the *significant* block vectors, and the block vectors that constitute an insignificant-natural block will be called as the *insignificant* block vectors. Block vectors that span any two adjacent significant- and insignificant-natural blocks are not desired, hence they can be called as the *undesired* block vectors. These terminologies are illustrated in figures 3(a) and (b) by using two segments extracted from the vector shown in figure 2(b). See Pant and Krishnan (2016) for more discussion on these terminologies.

3.2. $\ell^d_{2/p}$-RLS algorithm for enforcing block-sparse structure

Detection of the indices of the signal $\mathbf{x}$ corresponding to the QRS segments can be carried out by finding the indices of $x(n) - x(n-1)$ corresponding to the significant non-zero blocks. For extremely small values of the measurements M, i.e. for the values of M corresponding to the values of CR higher than 90%, the standard ℓ^d_p-RLS and $\ell^d_{2/p}$-RLS, and ℓ^{2d}_p-RLS algorithms tend to perform poorly. In such a case, enhancing the robustness of these algorithms is highly desired. Detecting the locations of the QRS segments is a key process in ECG monitoring applications, and robust detection of QRS segments would involve localization of the transient structures in the first-order difference of the ECG signal. It is known that parameter λ can be used to balance a trade-off between the signal fidelity and signal sparsity (Pant *et al* 2014); the larger the value of λ, the sparser the recovered signal. By inference, it can be expected that block sparse structure on the first-order difference of the signal can be enhanced by running the $\ell^d_{2/p}$-RLS algorithm (Pant and Krishnan 2016) with sufficiently large value of λ. Below, we illustrate this expectation by using an empirical observation on the ideal case of a pulse type signal. Experimental validation of the same using real ECG signals will be presented in section 4.1.

Consider a noisy signal of length $N = 1024$ and with a total of ten equal-width square pulses shown in figure 4(a). The two pulses at around $n = 900$ appear merged. The first-order difference of this signal can be readily shown to be near-sparse. Let Φ be a sparse measurement matrix with $M \approx 0.25N$, i.e. with CR = 75%, and $\mathbf{y}$ be the measurement vector obtained by using the signal in figure 4(a) and matrix Φ in (2). The $\ell^d_{2/p}$-RLS algorithm was applied several times for the reconstruction of a signal from $\mathbf{y}$, where the regularization parameter was set to $\lambda = 10^{-3}$ for nearly half of the reconstructions and $\lambda = 999$ was used for the other half of reconstructions. The rest of the parameters for the $\ell^d_{2/p}$-RLS algorithm for both of the cases were fixed to a reasonable set of constant values. Figures 4(b) and (c) show typical solutions obtained for $\lambda = 10^{-3}$ and $\lambda = 999$, respectively. As can be seen, all the transient structures are recovered in the vector plotted in figure 4(c); none of them are recovered in the vector plotted in figure 4(b). Even more, insignificant blocks are totally suppressed in the figure 4(c).

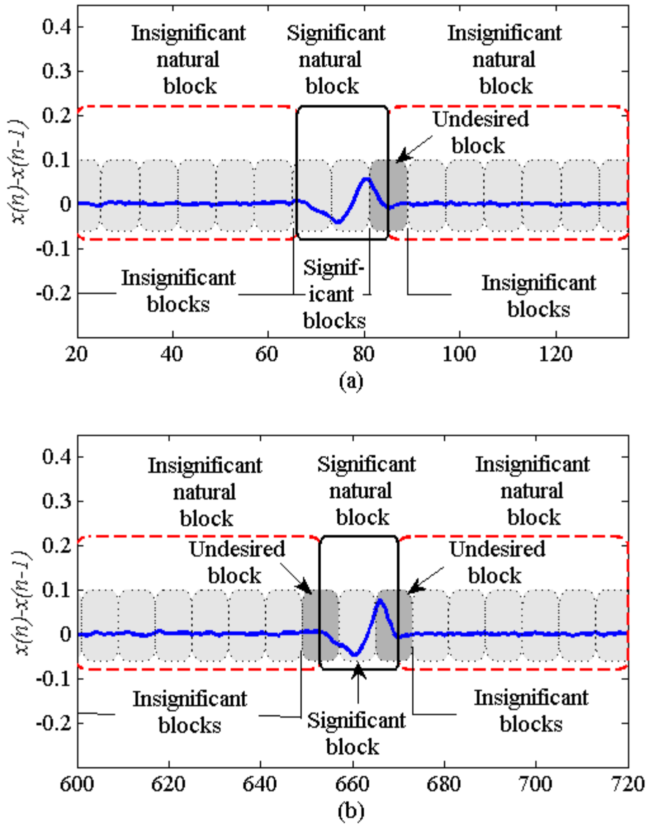

Figure 3. Division of the first-order difference vector into block vectors.

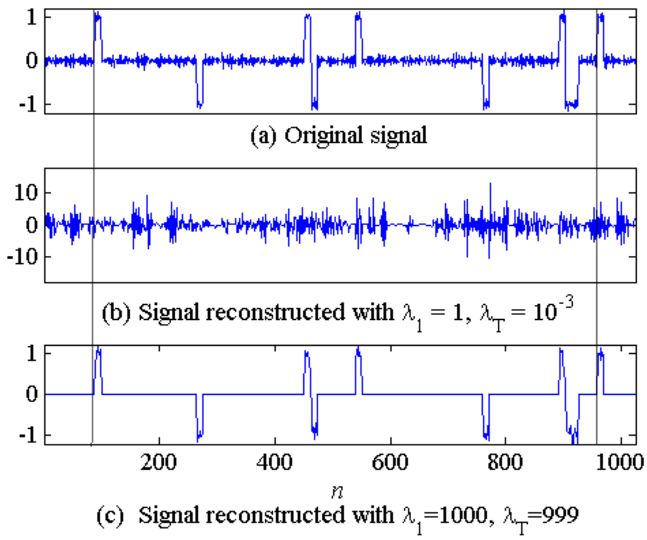

Figure 4. Original signal and solutions of the $\ell^d_{2/p}$-RLS algorithm: (a) noisy piece-wise constant signal, (b) vector $\mathbf{x}$ obtained with $\lambda = 10^{-3}$, (c) vector $\mathbf{x}$ obtained with $\lambda = 999$.

A question arises: 'Why does a large value of λ encourage a block-sparse solution?' We answer this question by looking at the topology of the objective function for large and small values of λ. In particular, we consider the topology of the objective function in (7) with $\epsilon = 0$ at the points represented by the vectors (signals) shown in figures 4(b) and (c) in the N-dimensional space.

Since the vectors plotted in figures 4(b) and (c) are solutions of the ℓ_p-RLS algorithm, they represent two minima of the objective function in (7) for $\epsilon = 0$. Let $\mathbf{x}_{\lambda_{\rm sm}}$ and $\mathbf{x}_{\lambda_{\rm lg}}$ denote the points in the N-dimensional space corresponding to the vectors shown in figures 4(b) and (c), respectively. In the N-dimensional space, a straight line passing through the points $\mathbf{x}_{\lambda_{\rm sm}}$ and $\mathbf{x}_{\lambda_{\rm lg}}$ can be represented as

$$\mathbf{x} = \mathbf{x}_c + \alpha \mathbf{x}_{\rm sl}, \tag{8a}$$

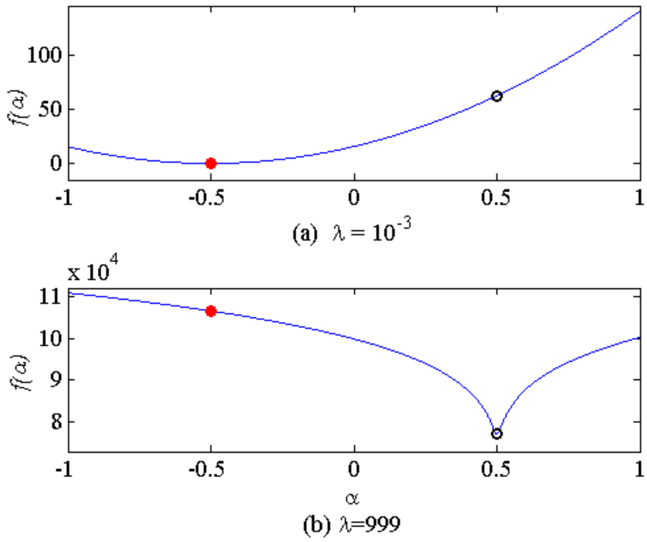

Figure 5. Function $f(\alpha)$ in (9): (a) $\lambda = 10^{-3}$, (b) $\lambda = 999$.

where the reference point $\mathbf{x}_c$ can be obtained as

$$\mathbf{x}_c = \frac{\mathbf{x}_{\lambda_{\rm sm}} + \mathbf{x}_{\lambda_{\rm lg}}}{2}, \tag{8b}$$

the vector $\mathbf{x}_{\rm sl}$ along the line represented by (8a) can be obtained as

$$\mathbf{x}_{\rm sl} = \mathbf{x}_{\lambda_{\rm lg}} - \mathbf{x}_{\lambda_{\rm sm}}, \tag{8c}$$

and α is a scalar variable. Using (8a), function $f(\mathbf{x})$ in (7) can be expressed as

$$f(\alpha) = \frac{1}{2}\,||\mathbf{y}_c + \alpha\mathbf{y}_{\rm sl}||_2^2 + \lambda f_r(\mathbf{x}_c + \alpha\mathbf{x}_{\rm sl}), \tag{9}$$

where $\mathbf{y}_c = \Phi\mathbf{x}_c - \mathbf{y}$ and $\mathbf{y}_{\rm sl} = \Phi\mathbf{x}_{\rm sl}$. Function $f(\alpha)$ can be used to evaluate the value of the objective function in (7) along the line connecting the solutions $\mathbf{x}_{\lambda_{\rm sm}}$ and $\mathbf{x}_{\lambda_{\rm lg}}$. Typical plots of $f(\alpha)$ for $\lambda = 999$ and $\lambda = 10^{-3}$ are shown in figures 5(a) and (b), respectively. In both plots, the values of $f(\alpha)$ for $\alpha = 0.5$ and $\alpha = -0.5$ are marked with a black circle and a solid red circle, respectively. By using (8b) and (8c) in (8a), it can be shown that $\alpha = 0.5$ corresponds to $\mathbf{x} = \mathbf{x}_{\lambda_{\rm lg}}$ (figure 4(c)) and $\alpha = -0.5$ corresponds to $\mathbf{x} = \mathbf{x}_{\lambda_{\rm sm}}$ (figure 4(b)). As can be seen in figure 5, $\alpha = 0.5$, i.e. the sparse vector $\mathbf{x}_{\lambda_{\rm lg}}$ shown in figure 4(c), is the minimizer of the function $f(\alpha)$ with $\lambda = 999$. Whereas $\alpha = -0.5$, i.e. the dense vector $\mathbf{x}_{\lambda_{\rm sm}}$ shown in figure 4(b), is the minimizer of the function $f(\alpha)$ with $\lambda = 10^{-3}$.

From the above discussion, it can be inferred that a high value of λ would be a better choice for using the $\ell^d_{2/p}$-RLS algorithm to determine the spikes and transient structures in the signal. More empirical evidence supporting this inference is presented in section 4.1.

3.3. Robust $\ell^d_{2/p}$-RLS algorithm

Undesired blocks of the first-order difference vector $\mathbf{x}^d$, which are illustrated in figure 3, occur if the beginning-time of a significant-natural block does not coincide with that of one of the signal blocks and/or if the ending-time of a significant-natural block does not coincide with that of one of the signal blocks. Because of the uncertainty in the locations and width of the significant-natural blocks of vector $\mathbf{x}^d$, the beginning or ending times of the significant-natural block would not coincide with that of the signal blocks; this can happen at least for a small number of significant-natural blocks.

In our simulations, which were carried out with high CR and with large values of λ, some of the significant-natural blocks were found to be missing in the estimated vector $\mathbf{x}^d$, regardless of the value of b used. A reasonable explanation for this is as follows. The undesired signal blocks can be expected to cause errors in the recovery of its adjoining significant-natural block. As a result, the natural blocks that have significant influence on the undesired signal blocks tend to get suppressed. Therefore, the robustness of the $\ell^d_{2/p}$-RLS algorithm to the suppression of non-zero blocks is highly desired. To this end, we select closely spaced values $b_{\tau_1}, b_{\tau_2}, \ldots, b_\tau$ of b, and we propose to run the $\ell^d_{2/p}$-RLS algorithm independently for a total of τ times with the selected values of b. Let $\mathbf{x}^d_{s,1}, \mathbf{x}^d_{s,2}, \ldots, \mathbf{x}^d_{s,\tau}$ be the absolute-value first-order difference vectors of the signals reconstructed by applying the $\ell^d_{2/p}$-RLS algorithm with $b = b_{\tau_1}, b_{\tau_2}, \ldots, b_\tau$, respectively. A typical plot of a vector $\mathbf{x}^d_{s,i}$ would look like the plot

Table 1. Robust $\ell_{2/p}^{d}$-RLS algorithm.

Step 1. Input: $b_1, b_2, \ldots, b_\tau, p, T, \epsilon_1, \epsilon_T, \lambda_1, \lambda_T, \Phi, \mathbf{y}$, E_t, L_b and r.
Step 2. Repeat the following for $i = 1, 2, \ldots, \tau$:
(i) select initializer $\mathbf{x}_s = \mathbf{0}$;
(ii) run the $\ell_{2/p}^{d}$-RLS algorithm (Pant and Krishnan 2016) with $b = b_i$, $p, T, \epsilon_1, \epsilon_T, \lambda_1, \lambda_T, \Phi, \mathbf{y}, E_t, L_b$ and r,
denote the resulting solution as $\mathbf{x}_{s,i}$.
Step 3. Compute the absolute-valued first-order difference $\mathbf{x}_{s,1}^{d}$, $\mathbf{x}_{s,2}^{d}, \ldots, \mathbf{x}_{s,\tau}^{d}$ of $\mathbf{x}_{s,1}, \mathbf{x}_{s,2}, \ldots, \mathbf{x}_{s,\tau}$, respectively.
Step 4. Compute $\mathbf{x}_s^*$ using (10).
Step 5. Output $\mathbf{x}_s^*$ and stop.

shown in figure 4(c) with few missing non-zero blocks. Usually, the non-zero blocks missed in one version of $\mathbf{x}_{s,i}^{d}$ are retained in the other versions. To recover all the non-zero blocks, a mean vector $\mathbf{x}_s^*$ can be constructed as

$$\mathbf{x}_s^* = \left[x_{s,1}^* \; x_{s,2}^* \; \cdots \; x_{s,N-1}^*\right]^T \tag{10a}$$

with

$$x_{s,i}^* = \frac{1}{\tau}\left(\frac{x_{s,1,i}^{d}}{\overline{x^{d}}_{s,1}} + \frac{x_{s,2,i}^{d}}{\overline{x^{d}}_{s,2}} + \cdots + \frac{x_{s,\tau,i}^{d}}{\overline{x^{d}}_{s,\tau}}\right) \tag{10b}$$

for $i = 1, 2, \ldots, N-1$, where $x_{s,j,i}^{d}$ is the absolute value of the ith component of $\mathbf{x}_{s,j}^{d}$ and $\overline{x^{d}}_{s,j}$ is the maximum value among the absolute values of the components of $\mathbf{x}_{s,j}^{d}$.

Error in the signal reconstruction can cause undesired blocks, usually of very small length, to appear in $\mathbf{x}_s^*$. However, such errors occur at random locations, and the mean operation (10) can not only suppress such errors but also emphasize the desired significant-natural blocks.

The procedure described above can be summarized as an algorithm, as shown in table 1. Input parameters p, $T, \epsilon_1, \epsilon_T, \lambda_1, \lambda_T, \Phi, \mathbf{y}, E_t, L_b$ and r are used to run the $\ell_{2/p}^{d}$-RLS algorithm in step 2.(ii). Detailed description of these parameters can be found in Pant and Krishnan (2016).

3.4. Post-processing and time-series estimation

The mean vector $\mathbf{x}_s^*$ obtained by using the robust $\ell_{2/p}^{d}$-RLS algorithm shown in table 1 can be smoothed using a smoothing operation $\mathrm{sm}(\cdot)$ as

$$\mathbf{x}_{\mathrm{sm}}^* = \mathrm{sm}(\mathbf{x}_s^*), \tag{11}$$

and it can be converted to a strictly block-sparse vector $\mathbf{u}_{\mathrm{sm}}$ as

$$\mathbf{u}_{\mathrm{sm}} = [u_{\mathrm{sm},1} \; u_{\mathrm{sm},2} \; \cdots \; u_{\mathrm{sm},N-1}]^T \tag{12a}$$

with

$$u_{\mathrm{sm},i} = \mathrm{sgn}\left\{\max(x_{\mathrm{sm},i} - th_i, 0)\right\} \tag{12b}$$

for $i = 1, 2, \ldots, N-1$, where $th_1, th_2, \ldots, th_{N-1}$ are small positive threshold values and the operation $\mathrm{sgn}\{\cdot\}$ returns 1 if the value inside the bracket is positive and it returns 0 if the value inside the bracket is zero.

Vector $\mathbf{u}_{\mathrm{sm}}$ obtained using (12) can be expected to contain unit rectangular pulses at the indices corresponding to the QRS segments. Erroneous $\mathbf{x}_{\mathrm{sm}}^*$ and $th_1, th_2, \ldots, th_{N-1}$ can cause some undesired pulses of small widths to appear near to the desired unit rectangular pulses. Sometimes, the desired unit rectangular pulse can also split into smaller pulses. The effect of this situation on the estimation of the time series can be mitigated by applying dilation (DIL) and erosion (ERO) operations described in Pant and Krishnan (2014a) on the vector $\mathbf{u}_{\mathrm{sm}}$. A description of these operations is as follows.

1 *Dilation.* One round of dilation operation on $\mathbf{u}_{\mathrm{sm}}$ yields a vector $\mathbf{u}_{\mathrm{sm}}^{dl}$ given by

$$\mathbf{u}_{\mathrm{sm}}^{dl} = \left[u_{\mathrm{sm},1}^{dl} \; u_{\mathrm{sm},2}^{dl} \; \cdots \; u_{\mathrm{sm},N-1}^{dl}\right]^T, \tag{13a}$$

where

$$u_{\mathrm{sm},i}^{dl} = \begin{cases} u_{\mathrm{sm},i} & \text{for } i = 1 \text{ and } N-1 \\ u_{\mathrm{sm},i}^{\mathrm{mm}x} & \text{otherwise} \end{cases}, \tag{13b}$$

and $u_{\mathrm{sm},i}^{\mathrm{mm}x}$ is the three-component moving maximum computed as

$$u_{\mathrm{sm},i}^{\mathrm{mm}x} = \max\{u_{\mathrm{sm},i-1}, u_{\mathrm{sm},i}, u_{\mathrm{sm},i+1}\} \tag{13c}$$

for $i = 2, 3, \ldots, N-2$.

2 *Erosion:* One round of erosion operation on $\mathbf{u}_{\mathrm{sm}}$ yields a vector $\mathbf{u}_{\mathrm{sm}}^{\mathrm{er}}$ given by

$$\mathbf{u}_{\mathrm{sm}}^{\mathrm{er}} = \left[u_{\mathrm{sm},1}^{\mathrm{er}} \ u_{\mathrm{sm},2}^{\mathrm{er}} \ \cdots \ u_{\mathrm{sm},N-1}^{\mathrm{er}}\right]^T, \tag{14a}$$

where

$$u_{\mathrm{sm},i}^{\mathrm{er}} = \begin{cases} u_{\mathrm{sm},i} & \text{for } i = 1 \text{ and } N-1 \\ u_{\mathrm{sm},i}^{\mathrm{mm}n} & \text{otherwise} \end{cases}, \tag{14b}$$

and $u_{\mathrm{sm},i}^{\mathrm{mm}n}$ is the three-component moving minimum computed as

$$u_{\mathrm{sm},i}^{\mathrm{mm}n} = \min\{u_{\mathrm{sm},i-1}, u_{\mathrm{sm},i}, u_{\mathrm{sm},i+1}\} \tag{14c}$$

for $i = 2, 3, \ldots, N-2$.

Once the selected rounds of DIL and ERO operations are applied in a suitable order, the resulting vector is expected to be a strictly sparse vector with rectangular pulses at the indices corresponding to the locations of QRS complexes. To reduce the rectangular pulses to impulses, several rounds of the erosion-without-termination (EWT) operations can be applied, where a one round of EWT operation on $\mathbf{u}_{\mathrm{sm}}$ yields a vector $\mathbf{u}_{\mathrm{sm}}^{\mathrm{ewt}}$ given by

$$\mathbf{u}_{\mathrm{sm}}^{\mathrm{ewt}} = \left[u_{\mathrm{sm},1}^{\mathrm{ewt}} \ u_{\mathrm{sm},2}^{\mathrm{ewt}} \ \cdots \ u_{\mathrm{sm},N-1}^{\mathrm{ewt}}\right]^T, \tag{15a}$$

where

$$u_{\mathrm{sm},i}^{\mathrm{ewt}} = \begin{cases} u_{\mathrm{sm},i} & \text{for } i = 1, N-1 \\ \max\{u_{\mathrm{sm},i}^{(1)}, u_{\mathrm{sm},i}^{(2)}\} & \text{otherwise} \end{cases} \tag{15b}$$

and $u_{\mathrm{sm},i}^{(1)}$ and $u_{\mathrm{sm},i}^{(2)}$ are three-component moving minimum and three-component impulse flag indexes, respectively, which can be obtained as

$$u_{\mathrm{sm},i}^{(1)} = \min\left\{u_{\mathrm{sm},i-1}, u_{\mathrm{sm},i}, u_{\mathrm{sm},i+1}\right\} \tag{15c}$$

$$u_{\mathrm{sm},i}^{(2)} = \min\left\{1 - u_{\mathrm{sm},i-1}, u_{\mathrm{sm},i}, 1 - u_{\mathrm{sm},i+1}\right\}, \tag{15d}$$

for $i = 2, 3, \ldots, N-2$.

A three-components operation applies in three consecutive components, and the three-component impulse flag index is 1 if the first and third components are zero-valued and the second component is unity-valued, otherwise it is 0. In multiple rounds of DIL, ERO, or EWT operations, the operation is carried out in the vector obtained from the previous round, except in the first round.

The EWT operation in (15) removes the first and last components from a block of consecutive unity-valued components. It stops short of removing an impulse, i.e. a block with only one unity valued component.

Several rounds of ERO operations would be effective for removing outlier impulses or rectangular pulses of very short duration. Several rounds of the DIL operation would be effective for merging the small rectangular pulses in $\mathbf{u}_{\mathrm{sm}}$ formed by splitting of a desired unit rectangular pulse. Subsequent application of sufficient rounds of the EWT operation in (15) would shrink a unit rectangular block into the impulse. The resulting vector $\mathbf{u}_{\mathrm{sm}}^{\mathrm{ewt}}$ can be expected to contain impulses at locations of the QRS segments. If $\tilde{m}_1, \tilde{m}_2, \ldots, \tilde{m}_\kappa$ denote the indices of the impulses in $\mathbf{u}_{\mathrm{sm}}^{\mathrm{ewt}}$, the estimated RR-interval time series can be obtained as

$$\hat{t}_s = [\hat{m}_1 \ \hat{m}_2 \ \cdots \ \hat{m}_{\kappa-1}]^T \tag{16a}$$

with

$$\hat{m}_i = \frac{\tilde{m}_{i+1} - \tilde{m}_i}{f_s}, \tag{16b}$$

where f_s is the sampling frequency used to acquire the signal $\mathbf{x}$ used in (2).

The post-processing and time-series estimation operations can be summarized as the PostP&TS-Est algorithm as shown in table 2. The mean vector $\mathbf{x}_s^*$ estimated by using the robust $\ell_{2/p}^d$-RLS algorithm, thresholds th_1

Table 2. PostP&TS-Est algorithm.

Step 1. Input: $\mathbf{x}_s^*$, th_1, th_2, …, th_{N-1}, N_{dil}, N_{ero}.
Step 2. Compute $\mathbf{x}_{\text{sm}}^*$ using (11).
Step 3. Compute $\mathbf{u}_{\text{sm}}$ using (12).
Step 4. Apply N_{ero} rounds of ERO operation (14) on $\mathbf{u}_{\text{sm}}$; denote resulting vector as $\mathbf{x}_{\text{sm}}^{\text{ero}}$.
Step 5. Apply N_{dil} rounds of DIL operation (13) on $\mathbf{x}_{\text{sm}}^{\text{ero}}$; denote resulting vector as $\mathbf{x}_{\text{sm}}^{\text{dil}}$.
Step 6. Apply N_{ewt} rounds of EWT operation (15) on $\mathbf{x}_{\text{sm}}^{\text{ewt}}$; denote resulting vector as $\mathbf{x}_{\text{sm}}^{\text{ewt}}$.
Step 7. Find indices of the unity-valued components of $\mathbf{x}_{\text{sm}}^{\text{ewt}}$; denote their indices as $\tilde{m}_1, \tilde{m}_2, \ldots, \tilde{m}_\kappa$.
Step 8. Compute vector $\hat{\mathbf{t}}_s$ using (16).
Step 9. Output $\hat{\mathbf{t}}_s$ and stop.

th_2, …, th_{N-1}, number of the rounds of DIL N_{dil}, ERO N_{ero}, and EWT N_{ewt} operations are supplied as input. A suitable method for smoothing, such as moving average and low-pass filtering, can be used as the operation $\text{sm}(\cdot)$ in step 2.

4. Simulation results

The ability of the basic $\ell_{2/p}^d$-RLS algorithm (Pant and Krishnan 2016) to reconstruct the ECG signals with an emphasized transient structure at the locations of QRS complexes is evaluated by conducting simulation 1. The proposed robust $\ell_{2/p}^d$-RLS algorithm in section 3.3 and table 1 is applied for the localization of QRS segments by conducting simulation 2. The performance of the robust $\ell_{2/p}^d$-RLS algorithm in conjunction with the Pan–Tompkins algorithm is evaluated by conducting simulations 3 and 4. The robust $\ell_{2/p}^d$-RLS algorithm is tested for its ability to detect correct QRS complexes by conducting simulation 5. The robust $\ell_{2/p}^d$-RLS algorithm is tested in conjunction with the PostP&TS-Est algorithm in table 2 for its ability to retain information for the estimation of HRV parameters by conducting simulation 6. Simulations 1–6 are detailed in sections 4.1–4.6, respectively.

For all the simulations, a sparse random measurement matrix of size $M \times N$ was constructed as follows: (a) construct a matrix Φ of size $M \times N$ with all-zero components, and (b) for all the columns of Φ, randomly select a total of 4 components and set to 1. Measurements $\mathbf{y}$ of a signal segment $\mathbf{x}$ were obtained as $\mathbf{y} = \Phi\mathbf{x}$. For a value of measurement M, the CR was computed as

$$\text{CR} = (N - M)/M \times 100\%. \tag{17}$$

The structural similarity index measure (SSIM) for an original signal segment $\mathbf{x}$ and corresponding reconstructed signal segment $\mathbf{x}^*$ was computed as (Wang *et al* 2004)

$$\text{SSIM}(\mathbf{x}, \mathbf{x}^*) = l \cdot c \cdot s, \tag{18}$$

where

$$l = \frac{2m_{\mathbf{x}}m_{\mathbf{x}^*} + 10^{-3}}{m_{\mathbf{x}}^2 + m_{\mathbf{x}^*}^2 + 10^{-3}}, \quad c = \frac{2\sigma_{\mathbf{x}}\sigma_{\mathbf{x}^*} + 10^{-3}}{\sigma_{\mathbf{x}}^2 + \sigma_{\mathbf{x}^*}^2 + 10^{-3}}, \quad s = \frac{\sigma_{\mathbf{x},\mathbf{x}^*} + 10^{-3}}{\sigma_{\mathbf{x}}\sigma_{\mathbf{x}^*} + 10^{-3}}. \tag{19}$$

In (19), $m_{\mathbf{x}}$ and $m_{\mathbf{x}^*}$ are mean values of $\mathbf{x}$ and $\mathbf{x}^*$, respectively, and $\sigma_{\mathbf{x}}$, $\sigma_{\mathbf{x}^*}$ and $\sigma_{\mathbf{x},\mathbf{x}^*}$ denote the standard deviation of $\mathbf{x}$, the standard deviation of $\mathbf{x}^*$ and the covariance of $\mathbf{x}$, $\mathbf{x}^*$, respectively.

The percentage root-mean-square difference (PRD) for an original signal segment $\mathbf{x}$ and corresponding reconstructed signal segment $\mathbf{x}^*$ was computed as

$$\text{PRD}(\mathbf{x}, \mathbf{x}^*) = (||\mathbf{x} - \mathbf{x}^*||_2) \,/\, ||\mathbf{x}||_2 \times 100, \tag{20}$$

where $\mathbf{x}$ and $\mathbf{x}^*$ are normalized so as to make their mean equal to zero before using in (20).

4.1. $\ell_{2/p}^d$-RLS algorithm for enforcing a block-sparse structure on the FoD of ECG signals (Simulation 1)

In section 3.2, the ability of the $\ell_{2/p}^d$-RLS algorithm to reconstruct the synthesized block-sparse signals by enforcing a block-sparse structure by using a large value of λ was studied. Here, we consider the ECG segments extracted from the MIT-BIH Arrhythmia database (Physionet 2018). The segment length N and the number of measurements M were selected as $N = 1024$ and $M = 0.05N$. This selection corresponds to an extremely

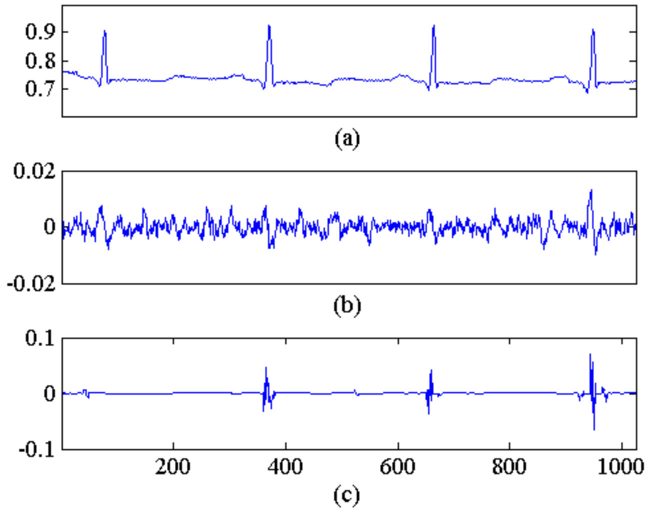

Figure 6. (a) Original ECG segment, (b) FoD vector of the segment reconstructed using the $\ell_{2/p}^{d}$-RLS ($\mathcal{S}_2$) algorithm, and (c) FoD vector of the segment reconstructed using $\ell_{2/p}^{d}$-RLS ($\mathcal{S}_1$) algorithm.

Table 3. Sparsity index $SP(\mathbf{x}^d)$ for $\ell_{2/p}^{d}$-RLS ($\mathcal{S}_1$) and $\ell_{2/p}^{d}$-RLS ($\mathcal{S}_2$) algorithms.

	$\ell_{2/p}^{d}$-RLS ($\mathcal{S}_1$)	$\ell_{2/p}^{d}$-RLS ($\mathcal{S}_2$)
Mean	0.6375	0.0301
Minimum	0.2972	0.0049
Maximum	0.7859	0.0635

high CR, i.e. CR $= 95\%$. A total $J = 633$ number of non-overlapping ECG segments were extracted from a record number `100m`. For each segment $\mathbf{x}$, the following steps were repeated a total of 25 times: (a) construct measurement matrix Φ and compute measurements $\mathbf{y}$, and (b) apply the $\ell_{2/p}^{d}$-RLS algorithm twice with two sets of the parameters $\mathcal{S}_1 = \{\epsilon_T = 10^{-7}, \lambda = 10^{10}, p = 10^{-6}\}$ and $\mathcal{S}_2 = \{\epsilon_T = 10^{-1}, \lambda = 10^{-2}, p = 1\}$. Thus, a total $633 \times 25 = 15\,825$ different reconstructions were carried out for each set of parameters. The FoD vectors of the solutions obtained for set $\mathcal{S}_1$ were observed to be similar to the one shown in figure 6(c), and that for set $\mathcal{S}_2$ were observed to be similar to the one shown in figure 6(b). The corresponding original ECG segment is shown in figure 6(a).

The sparsity of a FoD vector $\mathbf{x}^d$ was measured as

$$\mathrm{SP}(\mathbf{x}^d) = 1 - \frac{\sum_{n=1}^{N-1} \mathrm{sign}\left[\left(\left|x_n^d\right|\right)_{0.0001}\right]}{N-1},$$

where x_n^d is the nth component of $\mathbf{x}^d$, $\left|x_n^d\right|$ is the absolute value of x_n^d, $\left(\left|x_n^d\right|\right)_{0.0001}$ denotes the thresholded value obtained by setting it to zero if $\left|x_n^d\right| \leqslant 0.0001$, and the sign $[\cdot]$ operation gives 0 and 1 for zero-valued and positive-valued inputs, respectively. Mean, maximum, and minimum values of $SP\left(\mathbf{x}^d\right)$ for the $\ell_{2/p}^{d}$-RLS ($\mathcal{S}_1$) and $\ell_{2/p}^{d}$-RLS ($\mathcal{S}_2$) algorithms are shown in table 3.

These results indicate that small values of ϵ_T and p, and large value of λ encourage the $\ell_{2/p}^{d}$-RLS algorithm to enforce a block-sparse structure on the FoD of the reconstructed ECG segment. This situation can be expected to be favourable for finding the locations of QRS segments in an ECG signal. Therefore, the values similar to the ones in set $\mathcal{S}_1$ will be used for the realization of the $\ell_{2/p}^{d}$-RLS algorithm in the proposed robust $\ell_{2/p}^{d}$-RLS algorithm.

4.2. Localization of QRS segments by using the robust $\ell_{2/p}^{d}$-RLS algorithm (simulation 2)

A total of five values of b were selected as $b = 10, 12, 14, 16, 18$ and corresponding values of the number of blocks were set to $S = 72, 60, 51, 45, 40$, respectively. These values were selected so that the signal length $N = Sb + 1$ remains in the range from 715 to 721 . A signal segment $\mathbf{x}$ of length N was extracted from the MIT-BIH Arrhythmia database. The number of measurements M was selected as $M = 72$, which corresponds to CR $= 90\%$. After constructing a measurement matrix Φ and taking measurements $\mathbf{y}$, an estimation of the mean vector $\mathbf{x}_s^*$ was carried out by applying the robust $\ell_{2/p}^{d}$-RLS algorithm. The original signal and reconstructed FoD vectors were similar to that for the signal constructed by concatenating the first three segments of the first-channel in the record `100 m`, as shown in figure 7. The original signal is shown in figure 7(a), the absolute-valued

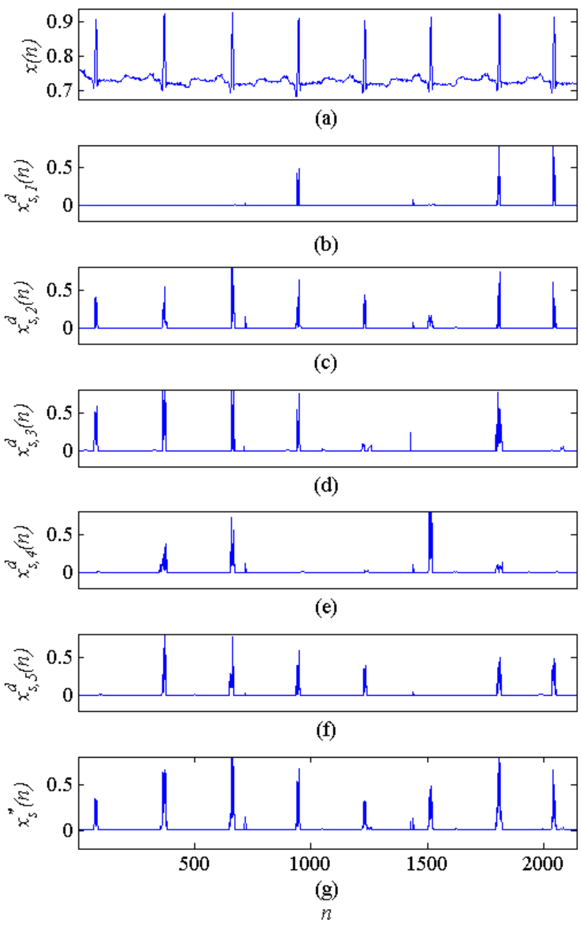

Figure 7. Original signal and reconstructed absolute-valued first-order differences $\mathbf{x}^d_{s,i}$: (a) original signal, (b) $\mathbf{x}^d_{s,1}$ with $b = 10$, (c) $\mathbf{x}^d_{s,2}$ with $b = 12$, (d) $\mathbf{x}^d_{s,3}$ with $b = 14$, (e) $\mathbf{x}^d_{s,4}$ with $b = 16$, (f) $\mathbf{x}^d_{s,5}$ with $b = 18$, (g) vector $\mathbf{x}^*_s$ obtained using $\mathbf{x}^d_{s,1}$, $\mathbf{x}^d_{s,2}$, $\mathbf{x}^d_{s,3}$, $\mathbf{x}^d_{s,4}$, and $\mathbf{x}^d_{s,5}$ in (10).

FoD vectors $\{\mathbf{x}^d_{s,i}\}$ of the signals reconstructed with $b = 10$, 12, 14, 16 and 18, which are observed in step 3 in table 1, are shown in figures 7(b)–(f), respectively. The mean vector $\mathbf{x}^*_s$ obtained in step 4 of the robust $\ell^d_{2/p}$-RLS algorithm is shown in figure 7(g). As can be seen, the mean vector has significantly large non-zero blocks for the indices corresponding to the QRS locations. The rest of the non-zero components are either very insignificant or very narrow in the width. This result indicates that the robust $\ell^d_{2/p}$-RLS algorithm can be useful for localizing spikes and transient structures in signals in CS applications with very high CR.

4.3. QRS detection using the robust $\ell^d_{2/p}$-RLS algorithm versus the Pan–Tompkins algorithm (simulation 3)

The DREAMER database (Katsigiannis and Ramzan 2017) contained ECG signals acquired by using a SHIMMER^{TM} on-body wireless sensor (Burns *et al* 2010) at the rate of 256 Hz. The database contains two channel ECG signals acquired from a total of 23 subjects while watching a total of 18 movies. The robust $\ell^d_{2/p}$-RLS algorithm was applied for the reconstruction of the ECG signals from their compressively sensed measurements. A total of $\tau = 5$ repetitions were carried out in step 2 of table 1 with $b_1 = 4$, $b_2 = 5$, $b_3 = 6$, $b_4 = 7$ and $b_5 = 8$. Typical ECG segments with irregular QRS complexes, noise-type artefacts and motion-type artefacts are shown in figures 8(a)(i), (b)(i) and (c)(i), respectively. Corresponding FoD vectors are shown in figures 8(a)(ii), (b)(ii) and (c)(ii). An average of the five versions of the reconstructed segments obtained after the five repetitions in step 2 of table 1 and corresponding FoD vectors, are shown in {figures 8(a)(iii) and (a)(iv)}, {figures 8(b)(iii) and (b)(iv)}, and {figures 8(c)(iii) and (c)(iv)}. For the plots shown in figures 8(a) and (b), CR = 90% was used, and for the plot shown in figure 8(c), CR = 85% was used. As can be seen, the robust $\ell^d_{2/p}$-RLS algorithm can be effective for recovering ECG segments with enhanced localization of QRS segments. SSIM and PRD for the plots shown in figures 8(a)–(c) were observed to be {0.9080, 57.9446}, {0.9131, 62.2055} and {0.9729, 25.8125}, respectively.

Next, Matlab code for the Pan–Tomkins algorithm (Pan and Tompkins 1985) was downloaded from Sedghamiz (2017), and it was used to detect QRS complexes from the ECG signals in the DREAMER database.

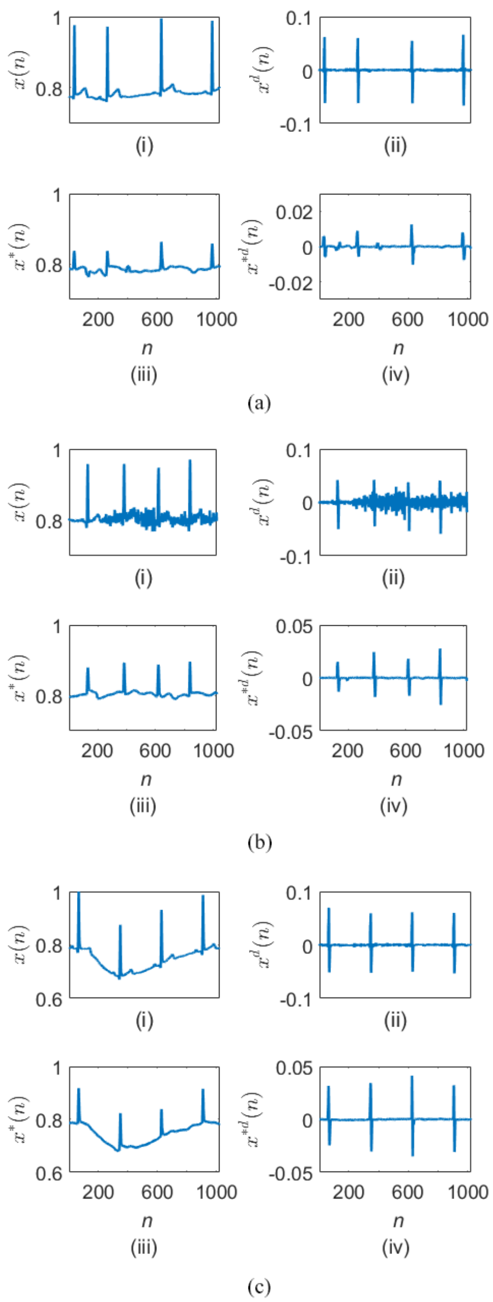

Figure 8. ECG segments with various irregularities and segments reconstructed using the robust $\ell_{2/p}^{d}$-RLS algorithm: (i) original segment, (ii) FoD of original segment, (iii) reconstructed segment, (iv) FoD of reconstructed segment. (a) Segment with irregular QRS complexes, CR = 90%. (b) Segment with noise-type artefact, CR = 90%. (c) Segment with motion-type artefact, CR = 85%.

The locations of the QRS complexes thus obtained will be called the original QRS locations. For the $\ell_{2/p}^{d}$-RLS algorithm, a total of $\tau = 5$ parallel reconstructions were carried out with $b = 4, 5, 6, 7, 8$. The signals obtained in step 2 of table 1 were averaged and the Pan–Tompkins algorithm was applied to estimate the QRS locations. Instances of correct detection of QRS location, erroneous detection of QRS location and erroneous miss of QRS location are called the instances of true positive (TP), false positive (FP), and false negative (FN), respectively. The number of TP, FP, and FN in the estimated QRS locations against the original QRS locations were counted. Sensitivity (Se) and positive predictivity (P+) were computed as

$$\mathrm{Se} = \frac{\mathrm{TP}}{\mathrm{TP} + \mathrm{FN}} \tag{21}$$

$$\mathrm{P}{+} = \frac{\mathrm{TP}}{\mathrm{TP} + \mathrm{FP}}. \tag{22}$$

A total of 108 ECG signals acquired from the first six subjects were considered, which contained a total of 15 356 QRS complexes as detected by the Pan–Tompkins algorithm (Sedghamiz 2017). Obtained TP, FP, FN, Se and

Table 4. TP, FP, FN, Se and P $+$ for the robust $\ell^d_{2/p}$-RLS algorithm and for the $\ell^d_{2/p}$-RLS algorithm with $b = 4, 5, 6, 7$ and 8.

Algorithm	TP	FP	FN	Se	P $+$
Robust $\ell^d_{2/p}$-RLS	14 877	293	478	0.9689	0.9807
$\ell^d_{2/p}$-RLS$(b = 4)$	14 602	288	753	0.9510	0.9807
$\ell^d_{2/p}$-RLS$(b = 5)$	14 728	294	654	0.9575	0.9804
$\ell^d_{2/p}$-RLS$(b = 6)$	14 847	374	508	0.9669	0.9754
$\ell^d_{2/p}$-RLS$(b = 7)$	14 927	499	428	0.9721	0.9677
$\ell^d_{2/p}$-RLS$(b = 8)$	14 918	784	437	0.9715	0.9501

P $+$ values for the robust $\ell^d_{2/p}$-RLS algorithm and these values for the segments obtained for the five iterations in step 2 of table 1 with $b = 4, 5, 6, 7$ and 8 are shown in table 4. As can be seen, larger values of b for the $\ell^d_{2/p}$-RLS algorithm has offered increase in Se, but decrease in P$+$. In this situation, the robust $\ell^d_{2/p}$-RLS algorithm has offered a balance between the undesired decrease in P$+$ and desired increase in Se.

4.4. Robustness to noise (simulation 4)

The robustness of the proposed robust $\ell^d_{2/p}$-RLS algorithm was evaluated in terms of SSIM computed using (18) for the reconstruction of noise corrupted ECG segments. A noise vector of length 1024 was constructed by drawing its components from a normal distributed random variable with zero mean and standard deviation equal to 0.03. The noise vector was added to an ECG segment of length 1024 extracted from the DREAMER database. The robust $\ell^d_{2/p}$-RLS, $\ell^d_{2/p}$-regularized least-squares ($\ell^d_{2/p}$-RLS) (Pant and Krishnan 2016), ℓ^d_p-regularized least-squares (ℓ^d_p-RLS) (Pant and Krishnan 2013), and block-sparse Bayesian learning-bound optimization (BSBL-BO) (Zhang *et al* 2013) algorithms were applied for the reconstruction of 10 000 different ECG segments from their compressively sensed measurements $\mathbf{y}$. The $\ell^d_{2/p}$-RLS, ℓ^d_p-RLS, and BSBL-BO algorithms have recently been found to be effective for the reconstruction of ECG signals from compressively sensed measurements (Zhang *et al* 2013, Pant and Krishnan 2013, 2016), where the BSBL-BO algorithm is based on encouraging block sparsity in order to promote temporal correlation on the signal (Zhang *et al* 2013).

SSIM obtained for the robust $\ell^d_{2/p}$-RLS, $\ell^d_{2/p}$-RLS and ℓ^d_p-RLS algorithms for the values of CR in the range from 86% to 94% is shown in figure 9(a). SSIM for the robust $\ell^d_{2/p}$-RLS and BSBL-BO algorithms is shown in figure 9(b). As can be seen, SSIM for the robust $\ell^d_{2/p}$-RLS algorithm is the largest relative to that for the other algorithms.

4.5. Evaluation of the $\ell^d_{2/p}$-RLS algorithm in terms of the correct QRS detection index (simulation 5)

The $\ell^d_{2/p}$-RLS algorithm was run with parameter sets $\mathcal{S}_1$ and $\mathcal{S}_2$ used in simulation 1 for enforcing a block-sparse structure and for encouraging signal fidelity, respectively. For the ℓ^d_p-RLS algorithm, the parameter set $\mathcal{S}_2$ was used. Involved reconstructions using the $\ell^d_{2/p}$-RLS algorithm for the proposed robust $\ell^d_{2/p}$-RLS algorithm were carried out by using the parameter sets $\mathcal{S}_1$. The signal vectors obtained by applying the robust $\ell^d_{2/p}$-RLS, $\ell^d_{2/p}$-RLS ($\mathcal{S}_1$), $\ell^d_{2/p}$-RLS ($\mathcal{S}_2$) and ℓ^d_p-RLS ($\mathcal{S}_2$) algorithms were supplied to the Pan–Tompkins algorithm for the detection of QRS locations. Thus, a total of four versions of the estimated QRS locations were obtained for the robust $\ell^d_{2/p}$-RLS, $\ell^d_{2/p}$-RLS ($\mathcal{S}_1$), $\ell^d_{2/p}$-RLS ($\mathcal{S}_2$) and ℓ^d_p-RLS ($\mathcal{S}_2$) algorithms. Each of the four estimated QRS locations for the record `100 m` in the MIT-BIH Arrhythmia database were compared with the true QRS locations for the same record downloaded from Physionet (2018). For each sequence of estimated QRS locations, the percentage of correctly detected QRS locations out of the total true QRS locations, called hits (HTs), and the percentage of wrongly detected QRS locations, called false alarms (FA), were computed. The correct QRS detection index (CQDI) was computed as

$$\mathrm{CQDI}_* = 2 \times [\alpha \cdot \mathrm{HT} - (1 - \alpha) \cdot \mathrm{FA}], \tag{23}$$

where parameter α can be in the range $0 \leqslant \alpha \leqslant 1$ and $\alpha = 0.5$ corresponds to $\mathrm{CQDI}_* = \mathrm{HT} - \mathrm{FA}$. In (23), $\{*\}$ is a placeholder for robust $\ell^d_{2/p}$, $\ell^d_{2/p}(\mathcal{S}_1)$, $\ell^d_{2/p}(\mathcal{S}_2)$ and $\ell^d_p(\mathcal{S}_2)$. The CQDI with $\alpha = 0.5$ for the robust $\ell^d_{2/p}$-RLS, $\ell^d_{2/p}$-RLS ($\mathcal{S}_1$), $\ell^d_{2/p}$-RLS ($\mathcal{S}_2$) and ℓ^d_p-RLS ($\mathcal{S}_2$) algorithms is shown in figure 10. As can be seen, the performance for the $\ell^d_{2/p}$-RLS ($\mathcal{S}_1$) algorithm is much better than that for the $\ell^d_{2/p}$-RLS ($\mathcal{S}_1$) and ℓ^d_p-RLS ($\mathcal{S}_2$) algorithms for CR $=$ 93%, 94%, 95% and 96%. The performance for the robust $\ell^d_{2/p}$-RLS algorithm is the best for CR $=$ 93%, 94%, 95% and 96%.

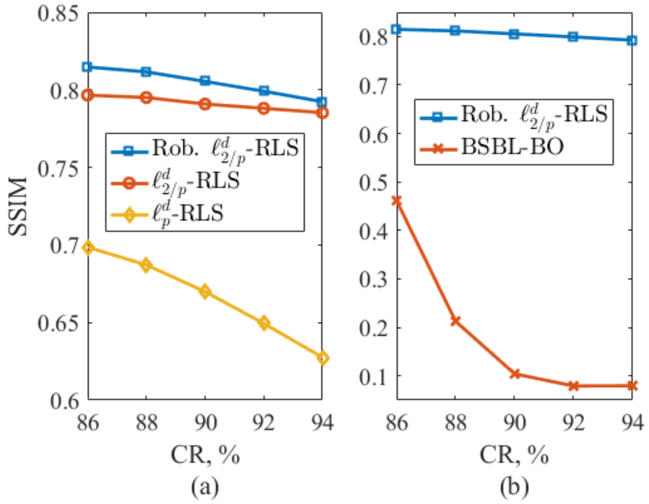

Figure 9. SSIM for CR = 86%, 88%, 90%, 92%, 94%: (a) SSIM for the robust $\ell^d_{2/p}$-RLS, $\ell^d_{2/p}$-RLS and ℓ^d_p-RLS algorithms, (b) SSIM for the robust $\ell^d_{2/p}$-RLS and BSBL-BO algorithms.

4.6. Estimation of HRV parameters by using the robust $\ell^d_{2/p}$-RLS and PostP&TS-Est algorithms (simulation 6)

The MIT-BIH Arrhythmia Database, consisting of 48 ECG records were downloaded from the Physionet website (Physionet 2018). Each record consisted of two-channel ECG signals, and the signals in the first channel were used. Six pairs of the values of block length b and number of blocks in a segment S were chosen as $\{b,S\} = \{10,60\}$, $\{12,45\}$, $\{14,37\}$, $\{16,27\}$, $\{18,24\}$ and $\{20,18\}$ so that the segment length $N = bS + 1$ remained in the range from 360 to 600. An ECG signal taken from Physionet was truncated so as to make its length equal to an integer multiple of N. The truncated ECG signal was divided into, say, total J, non-overlapping segments each of length N, and a matrix $\mathbf{X}$ of size $N \times J$ was constructed by using the ECG segments as its columns. The number of measurements M was selected so that the CR was approximately equal to 90%. A matrix Φ of size $M \times N$ was constructed and a matrix of measurement vectors $\mathbf{Y}$ was obtained as $\mathbf{Y} = \Phi\mathbf{X}$. The robust $\ell^d_{2/p}$-RLS algorithm shown in table 1 was applied with its step 2 implemented as shown in table 5. The solution matrix is denoted as $\mathbf{X}_s$, and it can be initialized as the zero matrix. The columns of $\mathbf{X}_s$ obtained after step 2.iii contain the reconstructed ECG segments. In step 2.iv of table 5, vector $\mathbf{x}_{s,i}$ can be constructed as

$$\mathbf{x}_{s,i} = \left[\mathbf{X}^T_{s,1}\ \mathbf{X}^T_{s,2}\ \cdots\ \mathbf{X}^T_{s,J}\right]^T \tag{24}$$

where $\mathbf{X}_{s,i}$ is the ith column of matrix $\mathbf{X}_s$.

The smoothing operation used in step 2 of the PostP&TS-Est algorithm shown in table 2 was realized by using the following procedure. First, vector $\mathbf{x}^*_s$ was passed through an FIR filter designed with a Hamming window of length 50. Second, the filtering operation was repeated on the vector obtained from the previous application of the filter. Finally, the above repetitive filtering was carried out for a total of ten times. Parameters $th_1, th_2, \ldots, th_{N-1}$ were supplied in step 1 of table 2 as the components of a vector $\mathbf{th}$ constructed using the following procedure: (a) vector $\mathbf{x}^*_{sm}$ was divided into non-overlapping block, each of length 150, samples, and the energy in each block of $\mathbf{x}^*_{sm}$ was computed, (b) the energy values were arranged as the components of a vector, and (b) the resulting vector was resampled, i.e. interpolated, at the value of the block length, i.e. 150. Consequently, a vector $\mathbf{th}$ of length $N - 1$ was obtained. Parameters N_{ero}, N_{dil}, and N_{ewt} were set to 10, 100 and 250, respectively.

For each of the records in the MIT-BIH Arrhythmia database: (a) an estimated time-series vector was obtained by first applying CS, then applying the robust $\ell^d_{2/p}$-RLS algorithm and finally applying the PostP&TS-Est algorithm shown in table 2, and (b) another estimated time-series vector was obtained by using the MATLAB implementation of the Pan–Tompkins algorithm.

The scaling exponent α obtained by using the de-trended fluctuation analysis, the standard deviation of average NN intervals (SDANN), the root mean square successive differences (r-MSSD) and the HRV index (HRVi) obtained using statistical analysis are recommended parameters for time-domain HRV assessment (John Camm 1996, Penzel *et al* 2003). An original RR-interval time series was downloaded from Physionet (2018), and estimated RR-interval time-series vectors were obtained for the Pan–Tompkins and CS-based methods for the 48 records taken from Physionet. The R programming-based HRV (RHRV) analysis package was downloaded from RHRV (2018), and it was used to compute parameters α, SDANN, r-MSSD, and HRVi from a time-series vector $\hat{\mathbf{t}}_s$. Let us use the symbols $\mathcal{O}$, $\mathcal{PT}$ and $\mathcal{PR}$ to represent a parameter (α, SDAAN, r-MSSD, or HRVi) com-

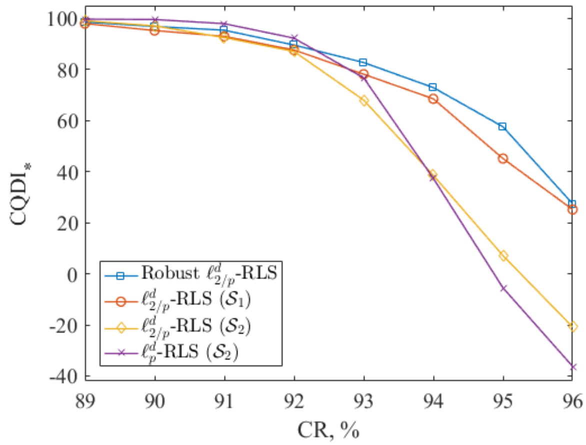

Figure 10. Correct QRS detection index (CQDI) for the robust $\ell^d_{2/p}$-RLS, $\ell^d_{2/p}$-RLS ($\mathcal{S}_1$), $\ell^d_{2/p}$-RLS ($\mathcal{S}_2$) and ℓ^d_{p}-RLS ($\mathcal{S}_2$) algorithms. $\{*\}$ is a placeholder for the robust $\ell^d_{2/p}$, $\ell^d_{2/p}$ ($\mathcal{S}_1$), $\ell^d_{2/p}$ ($\mathcal{S}_2$), or ℓ^d_{p}.

Table 5. Step 2 of the robust $\ell^d_{2/p}$-RLS algorithm for simulation 6.

Step 2. Repeat the following for $i = 1, 2, \ldots, \tau$:

(ii) select initializer matrix $\mathbf{X}_s = \mathbf{0}$;

(iii) repeat the following for $j = 1, 2, \ldots, J$:

(a) select the jth column of $\mathbf{Y}$ as $\mathbf{y}$,

(b) run the $\ell^d_{2/p}$-RLS algorithm (Pant and Krishnan 2016) with $b = b_i$, p, T, ϵ_1, ϵ_T, λ_1, λ_T, Φ, $\mathbf{y}$, E_t, L_b, and r,

(c) replace the jth column $\mathbf{X}_{s,j}$ of $\mathbf{X}_s$ by the solution obtained in step 2.iii.b;

(iv) construct solution signal $\mathbf{x}_{s,i}$ using (24).

puted from the original time series, the time-series obtained using Pan–Tompkins algorithm (Pan and Tompkins 1985), and that obtained based on the proposed CS-based method, respectively. The relative absolute error for the estimation of a parameter for the Pan–Tompkins algorithm, $\mathcal{E}^{PT}$, and that for the CS-based algorithm, $\mathcal{E}^{PR}$, were computed using

$$\mathcal{E}^{\mathrm{PT}} = \frac{|\mathcal{O} - \mathcal{PT}|}{\mathcal{O}}$$

and

$$\mathcal{E}^{\mathrm{PR}} = \frac{|\mathcal{O} - \mathcal{PR}|}{\mathcal{O}},$$

respectively. The difference error $\mathcal{E}_{\mathrm{Diff}}$ computed as

$$\mathcal{E}_{\mathrm{Diff}} = \mathcal{E}^{\mathrm{PR}} - \mathcal{E}^{\mathrm{PT}}$$

was used to compare the performance of the proposed algorithm with that of the Pan–Tompkins algorithm.

The scaling exponent α obtained for the original time series, $\mathcal{O}$, the time-series estimated by using the Pan–Tompkins algorithm, $\mathcal{PT}$, and that estimated based on the proposed CS-based method, $\mathcal{PR}$, for the 48 records is shown in table 6, and the obtained values of the parameters SDANN, r-MSSD, and HRVi for $\mathcal{O}$, $\mathcal{PT}$ and $\mathcal{PR}$ are shown in table 7 in the appendix. The negative values of $\mathcal{E}_{\mathrm{Diff}}$ indicate smaller error for the CS-based estimation algorithm relative to the Pan–Tompkins algorithm. The difference error in the range $-0.1 \leqslant \mathcal{E}_{\mathrm{Diff}} \leqslant 0.1$ can be deemed as an indicator of comparable performance of the CS-based and Pan–Tompkins-based estimation algorithms. In tables 6 and 7, the values of the difference error that satisfy the condition $\mathcal{E}_{\mathrm{Diff}} \leqslant 0.1$ are emphasized with bold, which are considered as the instances of comparable or better performance for the proposed CS-based method. As can be seen, out of a total 48 of records, the difference error for the estimation of scaling exponent α is within the range $\mathcal{E}_{\mathrm{Diff}} \leqslant 0.1$ for a total of 44 records. For the estimation of SDANN, it is within the range $\mathcal{E}_{\mathrm{Diff}} \leqslant 0.1$ for a total of 27 records. For the estimation of r-MSSD, it is within the range $\mathcal{E}_{\mathrm{Diff}} \leqslant 0.1$ for a total of 34 records. And, for the estimation of HRVi, it is within the range $\mathcal{E}_{\mathrm{Diff}} \leqslant 0.1$ for a total of 37 records. This indicates that the performance of the CS-based method is better than or comparable to that of the Pan–Tompkins algorithm.

Table 6. Scaling exponent α.

Record number	Original	Pan–Tompkins	CS-based	$\mathcal{E}_{\mathrm{Diff}}$
100m	0.8850	0.8816	0.8856	**− 0.0032**
101m	0.9158	0.9139	0.9148	**− 0.0010**
102m	0.4766	0.4594	0.5017	**0.0166**
103m	0.8113	0.8694	0.8727	**0.0041**
104m	0.6151	0.4207	0.6676	**− 0.2307**
105m	0.6140	0.8372	0.6708	**− 0.2710**
106m	1.0269	1.0530	0.9367	**0.0624**
107m	0.4027	0.5905	0.5451	**− 0.1127**
108m	0.8113	0.6567	0.7324	**− 0.0933**
109m	0.9097	0.9703	0.9559	**− 0.0158**
111m	0.8452	0.9657	0.6655	**0.0700**
112m	0.9499	1.0598	1.0296	**− 0.0318**
113m	0.6783	0.6784	0.5220	0.2303
114m	0.7541	0.6101	0.6700	**− 0.0794**
115m	0.7791	0.7572	0.7384	**0.0241**
116m	0.6355	0.8636	0.8066	**− 0.0897**
117m	0.9279	0.9639	0.7790	0.1217
118m	0.9967	1.2466	1.2503	**0.0037**
119m	0.7806	0.7927	0.7853	**− 0.0095**
121m	0.9560	1.2680	0.9516	**− 0.3218**
122m	1.2148	1.2191	1.2135	**− 0.0025**
123m	0.5791	0.5991	0.5761	**− 0.0294**
124m	1.1054	1.0949	1.0665	**0.0257**
200m	0.7694	0.7853	0.7879	**0.0034**
201m	1.0286	1.0508	1.0084	**− 0.0019**
202m	1.1265	1.1380	1.1013	**0.0122**
203m	0.6968	0.6390	0.6536	**− 0.0210**
205m	0.8680	0.8276	0.9053	**− 0.0036**
207m	1.2895	1.0548	1.0702	**− 0.0119**
208m	0.8178	0.8773	0.8500	**− 0.0334**
209m	1.1343	1.1634	1.1347	**− 0.0253**
210m	0.6120	0.5719	0.5972	**− 0.0413**
212m	0.7299	0.7881	0.7913	**0.0044**
213m	0.4997	0.5044	0.5336	**0.0584**
214m	0.7596	0.7511	0.7671	**− 0.0013**
215m	0.4549	0.4492	0.4641	**0.0077**
217m	0.7991	0.8070	0.7854	**0.0073**
219m	0.6089	0.7695	0.6193	**− 0.2467**
220m	0.7958	0.8268	0.8287	**0.0024**
221m	0.5868	0.5733	0.5662	**0.0121**
222m	0.7436	0.7567	0.6166	0.1532
223m	0.9709	1.0301	1.0683	**0.0393**
228m	0.7532	0.7815	0.8686	0.1156
230m	1.0350	1.0861	1.0846	**− 0.0014**
231m	0.9883	1.3493	0.8932	**− 0.2690**
232m	0.6251	0.5287	0.4980	**0.0491**
233m	0.6305	0.5635	0.6087	**− 0.0717**
234m	0.9733	1.0987	1.1014	**0.0028**

Table 7. Parameters SDANN, RMSSD and HRV for the original and estimated RR-interval time-series.

Record name	SDANN				r-MSSD				HRVi			
	$\mathcal{O}$	$\mathcal{PT}$	$\mathcal{PR}$	$\mathcal{E}_{\text{Diff}}$	$\mathcal{O}$	$\mathcal{PT}$	$\mathcal{PR}$	$\mathcal{E}_{\text{Diff}}$	$\mathcal{O}$	$\mathcal{PT}$	$\mathcal{PR}$	$\mathcal{E}_{\text{Diff}}$
100m	18.277	16.863	18.121	**−0.0688**	35.667	35.585	37.105	**0.0380**	10.088	10.239	9.742	**0.0193**
101m	49.398	46.262	49.508	**−0.0613**	39.069	39.860	38.840	**−0.0144**	15.509	17.232	16.411	**−0.0529**
102m	3.238	2.892	3.177	**−0.0880**	38.228	43.783	31.059	**0.0422**	9.653	10.597	9.524	**−0.0844**
103m	9.747	13.939	10.339	**−0.3693**	39.635	33.410	33.631	**−0.0056**	12.439	12.695	12.319	**−0.0109**
104m	8.808	3.070	4.925	**−0.2106**	63.685	69.121	65.632	**−0.0548**	9.623	11.221	11.983	**0.0792**
105m	28.700	29.242	33.421	0.1456	56.728	30.977	51.027	**−0.3534**	10.852	9.754	10.566	**−0.0748**
106m	86.129	83.760	55.040	0.3335	197.108	190.809	152.617	0.1938	36.133	34.298	31.958	**0.0648**
107m	2.616	3.316	1.553	0.1388	33.382	32.949	46.333	0.3750	8.686	8.356	9.018	**0.0002**
108m	52.731	82.037	59.093	**−0.4351**	95.992	83.671	123.322	0.156	23.054	23.887	22.419	**−0.0086**
109m	11.842	12.329	11.670	**−0.0266**	38.999	35.646	36.302	**−0.0168**	9.423	9.660	9.552	**−0.0115**
111m	17.206	16.283	13.078	0.1863	36.912	34.658	76.611	1.01444	10.912	11.257	13.085	0.1675
112m	14.357	14.440	13.829	**0.0310**	17.993	17.852	21.169	0.1687	6.240	6.489	6.787	**0.0478**
113m	27.628	27.628	27.149	**0.0173**	92.614	92.574	114.014	0.2306	21.518	22.049	23.939	**0.0878**
114m	95.101	88.739	51.745	0.3890	67.071	114.617	183.238	1.0231	25.125	27.979	32.490	0.1795
115m	20.010	19.506	21.267	**0.0376**	72.771	71.676	71.953	**−0.0038**	19.440	21.163	19.917	**−0.0641**
116m	17.958	18.030	14.045	0.2139	24.424	23.549	27.889	0.1060	6.965	7.373	7.096	**−0.0398**
117m	13.730	12.957	16.227	0.1256	36.242	33.193	166.532	3.5109	8.612	8.570	17.904	1.0741
118m	42.231	41.475	39.590	**0.0446**	40.073	35.759	38.183	**−0.0605**	14.814	15.357	14.880	**−0.0322**
119m	9.314	71.456	26.152	**−4.8641**	77.654	128.636	116.655	**−0.1543**	9.550	10.610	11.288	**0.0710**
121m	74.992	73.088	18.934	0.7221	31.730	20.009	39.979	**−0.1094**	12.793	12.456	10.898	0.1218
122m	12.738	12.772	14.184	0.1108	19.112	18.983	20.843	**0.0838**	11.246	11.204	11.622	**0.0297**
123m	13.605	13.321	15.030	**0.0839**	103.693	102.604	101.741	**0.0083**	26.561	29.115	31.553	**0.0918**
124m	54.550	54.828	37.325	0.3107	46.381	46.733	46.203	**−0.0037**	22.042	21.446	20.827	**0.0281**
200m	33.989	54.226	16.750	**−0.0882**	180.426	149.439	173.291	**−0.1322**	34.106	30.968	27.163	0.1116
201m	242.203	242.482	215.486	0.1092	192.580	202.211	152.901	0.1560	41.474	44.486	37.932	**0.0128**
202m	242.295	241.748	222.179	**0.0808**	110.666	110.519	110.347	**0.0016**	28.853	30.108	33.483	0.1170
203m	37.517	33.943	28.021	0.1578	177.806	172.944	179.203	**−0.0195**	36.118	38.322	36.246	**−0.0575**
205m	37.331	36.034	30.721	0.1423	23.732	27.853	27.881	**0.0012**	8.873	9.042	9.129	**0.0098**
207m	128.630	103.510	125.075	**−0.1677**	85.466	98.721	105.721	**0.0819**	22.333	22.321	19.092	0.1446
208m	30.673	30.465	26.823	0.1187	128.917	131.641	134.393	**0.0213**	17.469	18.215	18.061	**−0.0088**
209m	35.268	35.329	37.419	**0.0593**	53.167	50.430	54.282	**−0.0305**	10.452	10.844	9.969	**0.0087**
210m	9.876	8.550	7.278	0.1288	118.359	119.209	116.891	**0.0052**	21.848	21.186	21.651	**−0.0213**
212m	19.695	19.178	15.597	0.1818	29.047	26.181	27.591	**−0.0485**	11.361	11.167	10.672	**0.0436**
213m	8.945	9.022	7.911	0.1070	39.020	31.989	33.223	**−0.0316**	5.280	5.169	5.908	**0.0979**
214m	14.752	12.675	13.007	**−0.0225**	85.903	87.703	90.281	**0.0300**	17.835	15.585	18.490	**−0.0894**
215m	4.886	4.480	4.975	**−0.0649**	49.267	47.231	50.126	**−0.0239**	9.377	8.939	10.635	**0.0874**
217m	15.686	17.029	25.526	0.5417	74.030	72.152	75.126	**−0.0106**	12.262	12.414	13.916	0.1225
219m	11.473	67.729	35.611	**−2.7994**	148.825	173.736	151.754	**−0.1477**	24.618	27.739	22.506	**−0.0410**
220m	34.022	34.120	36.943	**0.0830**	57.527	58.153	58.400	**0.0043**	14.962	14.667	14.840	**−0.0116**
221m	23.421	23.051	25.807	**0.0861**	179.779	180.894	173.396	**0.0293**	24.705	25.987	26.736	**0.0303**
222m	68.923	73.068	44.119	0.2997	163.094	164.299	214.500	0.3078	33.045	36.400	51.606	0.4602
223m	34.023	31.241	34.228	**−0.0757**	62.482	64.472	64.272	**−0.0032**	9.500	9.632	9.837	**0.0216**
228m	23.623	22.605	104.380	3.3755	142.036	139.313	268.627	0.8721	20.734	21.408	39.000	0.8485
230m	67.054	66.887	64.065	**0.0421**	30.391	28.360	30.363	**−0.0659**	25.614	25.625	26.310	**0.0267**
231m	9.030	168.897	82.057	**−9.6168**	55.537	82.968	139.507	1.0180	11.529	16.978	16.767	**−0.0183**
232m	18.122	13.309	29.493	0.3619	126.661	130.006	202.075	0.5690	6.980	6.720	10.787	0.5082
233m	11.531	15.104	10.380	**−0.2100**	133.570	153.024	130.723	**−0.1243**	8.152	7.230	8.538	**−0.0657**
234m	10.113	9.977	9.185	**0.0783**	21.477	19.279	20.973	**−0.0789**	5.985	5.514	5.775	**−0.0436**

5. Conclusion

A new CS-based method for the acquisition of ECG signals and for the estimation of RR-interval time series was proposed. The method is based on using CS for ECG compression in the biosensor and the use of a new robust $\ell_{2/p}^{d}$-RLS algorithm for the estimation of the time indices of the locations of the QRS segments. The robust $\ell_{2/p}^{d}$-RLS algorithm is useful for estimating the locations of QRS segments from the measurements with very high CR, hence it allows significantly increasing the CR and reducing the consumption of energy in the sensor. The robust $\ell_{2/p}^{d}$-RLS algorithm runs efficiently with the hardware and software resources typically available for telemonitoring systems. Simulation results demonstrate that the performance of the proposed CS-based method for the estimation of HRV parameters is comparable with that based on the Pan–Tompkins algorithm.

Acknowledgment

The authors would like to thank the Canada Research Chairs program for supporting this research.

Appendix. Parameters SDANN, r-MSSD, HRVi and difference error

Values of the parameters SDANN, r-MSSD and HRVi for the original time series $\mathcal{O}$, for the time series estimated by using the Pan–Tompkins algorithm $\mathcal{PT}$, and for the time series estimated by using the proposed robust CS-based algorithm $\mathcal{PR}$, discussed in section 4.6, are shown in table 7.

References

Arzeno N M, Deng Z-D and Poon C-S 2008 Analysis of first-derivative based QRS detection algorithms *IEEE Trans. Biomed. Eng.* **55** 478–84
Burns A, Greene B R, McGrath M J, O'Shea T J, Kuris B, Ayer S M, Stroiescu F and Cionca V 2010 SHIMMER– a wireless sensor platform for noninvasive biomedical research *IEEE Sensors J.* **10** 1527–34
Candes E, Romberg J and Tao T 2006 Robust uncertainty principles: exact signal reconstruction from highly incomplete frequency information *IEEE Trans. Inf. Theory* **52** 489–509
Candes E and Tao T 2006 Near-optimal signal recovery from random projections: universal encoding strategies *IEEE Trans. Inf. Theory* **52** 5406–25
Dipu C J and Lian Y 2015 A joint QRS detection and data compression scheme for wearable sensors *IEEE Trans. Biomed. Eng.* **62** 165–75
Dixon A M R, Allstot E G, Gangopadhyay D and Allstot D J 2012 Compressed sensing system considerations for ECG and EMG wireless biosensors *IEEE Trans. Biomed. Circuits Syst.* **6** 156–66
Donoho D L 2006 Compressed sensing *IEEE Trans. Inf. Theory* **52** 1289–306
Eldar Y C and Mishali M 2009 Robust recovery of signals from a structured union of subspaces *IEEE Trans. Inf. Theory* **55** 5302–16
Eldar Y C, Kuppinger P and Bolcskei H 2010 Block-sparse signals: uncertainty relations and efficient recovery *IEEE Trans. Signal Process.* **58** 3042–54
Gangopadhyay D, Allstot E G, Dixon A M R, Natarajan K, Gupta S and Allstot D J 2014 Compressed sensing analog front-end for bio-sensor applications *IEEE J. Solid-State Circuits* **49** 426–38
Goudar V and Potkonjak M 2013 Fault-tolerant and low-power sampling schedules for localized BASNs *IEEE J. Emerg. Sel. Top. Circuits Syst.* **3** 86–95
Hamilton P S and Tompkins W J 1986 Quantitative investigation of QRS detection rules using the MIT/BIH Arrhythmia database *IEEE Trans. Biomed. Eng.* **BME-33** 1157–65
John Camm A *et al* 1996 Heart rate variability: standards of measurement, physiological interpretation, and clinical use *Eur. Heart J.* **17** 354–81
Jovanov E, Milenkovic A, Otto C and Groen P C D 2005 A wireless body area network of intelligent motion sensors for computer assisted physical rehabilitation *J. Neuroeng. Rehabil.* **2** 1–10
Katsigiannis S and Ramzan N 2017 DREAMER: a database for emotion recognition through EEG and ECG signals from wireless low-cost off-the-shelf devices *IEEE J. Biomed. Health Inform.* **22**
Köhler B-U, Hennig C and Orglmeister R 2002 The principles of software QRS detection *IEEE Eng. Med. Biol. Mag.* **21** 42–57
Lin C-T *et al* 2010 An intelligent telecardiology system using a wearable and wireless ECG to detect atrial fibrillation *IEEE Trans. Inf. Technol. Biomed.* **14** 726–33
Liu B, Zhang Z, Xu G, Fan H and Fu Q 2014 Energy efficient telemonitoring of physiological signals via compressed sensing: a fast algorithm and power consumption evaluation *Biomed. Signal Process. Control* **11** 80–8
Mamaghanian H, Khaled N, Atienza D and Vandergheynst P 2011 Compressed sensing for real-time energy-efficient ECG compression on wireless body sensor nodes *IEEE Trans. Biomed. Eng.* **58** 2456–66
National Health Expenditure Trends 2014 *Technical Report* Canadian Institute for Health Information
Noshadi H, Dabiri F, Ahmadian S, Amini N and Sarrafzadeh M 2013 Hermes: mobile system for instability analysis and balance assessment *ACM Trans. Embedded Comput. Syst.* **12** 57:1–57:24
Pan J and Tompkins W J 1985 A real-time QRS detection algorithm *IEEE Trans. Biomed. Eng.* **BME-32** 230–6
Pant J K and Krishnan S 2013 Reconstruction of ECG signals for compressive sensing by promoting sparsity on the gradient *Proc. IEEE Intl. Symp. Circuits and Syst.* pp 993–7
Pant J K and Krishnan S 2014a Foot gait time series estimation based on support vector machine *Proc. Intr. IEEE Eng. Med. Biol. Soc. Conf. (EMBC)* pp 6410–3
Pant J K and Krishnan S 2014b Compressive sensing of electrocardiogram signals by promoting sparsity on the second-order difference and by using dictionary learning *IEEE Trans. Biomed. Circuits Syst.* **8** 293–302

Pant J K and Krishnan S 2016 Compressive sensing of foot gait signals and its application for the estimation of clinically relevant time series *IEEE Trans. Biomed. Eng.* **63** 1401–15

Pant J K, Lu W-S and Antoniou A 2014 New improved algorithms for compressive sensing based on ℓ_p norm *IEEE Trans. Circuits Syst.* II **61** 198–202

Penzel T, Kantelhardt J W, Grote L, Peter J-H and Bunde A 2003 Comparison of detrended fluctuation analysis and spectral analysis for heart rate variability in sleep and sleep apnea *IEEE Trans. Biomed. Eng.* **50** 1143–51

Physionet 2018 MIT-BIH arrhythmia database www.physionet.org/physiobank/database/mitdb/

Purdy L 2015 Health care outlook *Technical Report* Deloitte Canada

RHRV 2018 Heart rate variability analysis of ECG data https://cran.r-project.org/web/packages/RHRV/index.html

Sedghamiz H 2017 Complete pan tompkins implementation ECG QRS detector http://mathworks.com/matlabcentral/fileexchange/45840-complete-Pan–Tompkins-implementation-ecg-qrs-detector/content/pan tompkin.m

Stojnic M, Parvaresh F and Hassibi B 2009 On the reconstruction of block-sparse signals with an optimal number of measurements *IEEE Trans. Signal Process.* **57** 3075–85

Suppappola S and Sun Y 1994 Nonlinear transforms of ECG signals for digital QRS detection: a quantitative analysis *IEEE Trans. Biomed. Eng.* **41** 397–400

Wang Z, Bovik A C, Sheikh H R and Simoncelli E P 2004 Image quality assessment: from error visibility to structural similarity *IEEE Trans. Image Process.* **13** 600–12

Xue Q, Hu Y H and Tompkins W J 1992 Neural-network-based adaptive matched filtering for QRS detection *IEEE Trans. Biomed. Eng.* **39** 317–29

Zhang Z, Jung T-P, Makeig S and Rao B D 2013 Compressed sensing for energy-efficient wireless telemonitoring of noninvasive fetal ECG via block sparse Bayesian learning *IEEE Trans. Biomed. Eng.* **60** 300–9